Effects of preorganization in the chelation of UO22+ by hydroxamate ligands: cyclic PIPO– vs linear NMA–

Alejandra Sornosa-Ten, Pawel Jewula, Tamas Fodor, Stéphane Brandès, Vladimir Sladkov, Yoann Rousselin, Christine Stern, Jean-Claude Chambron, Michel Meyer

New Journal of Chemistry **2018**, *42*, 7765–7779 – **DOI:** 10.1039/c8nj00166a

Effects of preorganization in the chelation of UO_2^{2+} by hydroxamate ligands: cyclic $PIPO^-$ *vs* linear NMA^- †

Received 10th January 2018,
Accepted 12th February 2018

DOI: 10.1039/c8nj00166a

Alejandra Sornosa-Ten,[a] Pawel Jewula,[a] Tamas Fodor,[a] Stéphane Brandès,[a] Vladimir Sladkov,[b] Yoann Rousselin,[a] Christine Stern,[a] Jean-Claude Chambron*[a] and Michel Meyer*[a]

Many siderophores incorporate as bidentate chelating subunits linear and more seldomly cyclic hydroxamate groups. In this work, a comparative study of the uranyl binding properties in aqueous solution of two monohydroxamic acids, the prototypical linear *N*-methylacetohydroxamic acid (NMAH) and the cyclic analog 1-hydroxypiperidine-2-one (PIPOH), has been carried out. The complex $[UO_2(PIPO)_2(H_2O)]$ crystallized from slightly acidic water solutions (pH < 5), and its molecular structure was determined by X-ray diffraction. The uranyl speciation in the presence of both ligands has been thoroughly investigated in 0.1 M KNO_3 medium at 298.2 K by the combined use of four complementary techniques, *i.e.*, potentiometry, spectrophotometry, Raman spectroscopy, and affinity capillary electrophoresis. Preorganization of the hydroxamate ligand for chelation by incorporation into a cyclic structure, as in $PIPO^-$, results in gaining nearly one order of magnitude in the formation constants of the uranyl complexes of 1:1 and 1:2 metal/ligand stoichiometries.

Introduction

The uranyl dication (UO_2^{2+}) is the thermodynamically stable and water soluble form of uranium(VI). It is found in natural uranium ores such as autunite (an uranyl phosphate) and carnotite (an uranyl vanadate), and therefore in the vicinity of uranium mines. Therefore, it is of utmost importance to delineate how uranyl is solubilized and transported in contaminated soils.[1-4] A possible lead, which has been put forward and subsequently explored, is the role of siderophores.[5-10] These natural chelators are secreted by microorganisms present in the pedological layer in order to dissolve and capture Fe^{3+} from iron oxo-hydroxides for their own supply, ferrisiderophores being recognized back by specific receptors anchored into the cytoplasmic membrane.[11-14]

Many siderophores feature at least one, but often three like in desferrioxamine B (DFB), hydroxamic acid groups ($R^1C(=O)N(OH)R^2$) as metal binding units. Their deprotonated hydroxamate form plays the role of an anionic bidentate *O*-chelating fragment. Most of the hydroxamic functions are, in fact, derived from *N*-methylacetohydroxamic acid (NMAH; R^1 = R^2 = Me), which can feature *cis* (*Z*) and *trans* (*E*) conformations by rotation about the carbon-nitrogen bond (Chart 1), the latter being useless for chelation.[15]

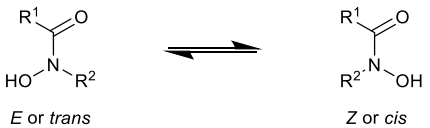

R^1	R^2	
H	H	FHAH
Me	H	AHAH
Me	Me	NMAH
Me	Ph	NPAH
Ph	H	BHAH
(2-OH)Ph	H	SHAH
Ph	Ph	PBAH
(4-*i*Pr)Ph	Ph	IBPHAH

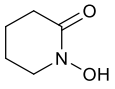

PIPOH

Chart 1 Molecular formula and acronym of monohydroxamic acids discussed herein

After a long lasting controversy in the literature, it was recently ascertained that the *E* rotamer of both NMAH and its conjugated base NMA^- prevail in aqueous solution and at room temperature in a nearly 3:1 and 9:1 ratio over a large concentration range, respectively.[15-16] In contrast, the *E*/*Z* concentration ratio was found to be strongly concentration dependent in less-polar media like chloroform, with predominance of the *Z* form in dilute solutions possibly stabilized through intramolecular C=O···HO–N hydrogen bonding, while at higher concentrations the *E* isomer is favored,

[a] Institut de Chimie Moléculaire de l'Université de Bourgogne (ICMUB), UMR 6302, CNRS, Université Bourgogne–Franche-Comté, 9 avenue Alain Savary, BP 47870, 21078 Dijon Cedex, France.
E-mail: michel.meyer@u-bourgogne.fr; Tel: +33 3 80 39 37 16
[b] Institut de Physique Nucléaire d'Orsay (IPNO), UMR 8608, CNRS, Université Paris Sud, 15 rue George Clemenceau, 91406 Orsay Cedex, France.

† Electronic Supplementary Information (ESI) available: crystallographic, diffuse reflectance, IR, and Raman data for the uranyl complexes; protonation constants for NMA^-; calorimetric data for the protonation of NMA^- and $PIPO^-$; values of the hydrolysis constants of UO_2^{2+}; capillary electrophoregrams for the UO_2^{2+}/PIPOH system; ^1H NMR data for the UO_2^{2+}/NMAH system. CCDC 1579042. For ESI and crystallographic data in CIF see DOI: 10.1039/c8nj00166a

suggesting intermolecular chain-type aggregation.[17] The interconversion kinetics in water, which is slow on the NMR time scale, has been elucidated independently by two groups using either 2D exchange-correlated (EXSY)[15] or variable-temperature ^{1}H NMR spectroscopy[18] ($\Delta G^{\neq}_{Z\rightarrow E}$ = 68.0 kJ mol^{-1} and $\Delta G^{\neq}_{E\rightarrow Z}$ = 70.6 kJ mol^{-1} for NMAH, $\Delta G^{\neq}_{Z\rightarrow E}$ = 73.6 kJ mol^{-1} and $\Delta G^{\neq}_{E\rightarrow Z}$ = 79.2 kJ mol^{-1} for NMA$^-$ at 300 K).

Today, the coordination chemistry of primary (R^2 = H) and secondary (R^2 = alkyl or aryl group) hydroxamates with various metal-derived cations, including actinides, is rather well-known.[19-20] In this respect, it is worth to mention that formo- (FHAH; R^1 = R^2 = H) and acetohydroxamic acids (AHAH; R^1 = Me, R^2 = H) have been implemented in advanced PUREX flow-sheets, especially to control the oxidation states of neptunium(VI) and plutonium(IV) during the liquid-liquid partitioning process.[21-22] Both primary hydroxamic acids selectively reduce NpO_2^{2+} and Pu^{4+} but have no redox activity in presence of UO_2^{2+}, thus enabling the selective recovery of uranium(VI) in the organic phase. Recently, the crystal structure of two mono- and bischelated uranyl complexes of *N*-methylacetohydroxamate of $[UO_2(NMA)(NO_3)(H_2O)_2]$ and $[UO_2(NMA)_2(H_2O)]$ composition have been described.[15] In both compounds, the uranium atom is surrounded by five equatorial and essentially planar oxygen atoms provided by the bidentate hydroxamate and the additional monodentate ligands (H_2O and/or NO_3^-). Interestingly, both environments give rise to distinct IR and Raman spectral signatures for the U=O stretches, allowing to easily distinguish them from the pentaaquo UO_2^{2+} cation. Most remarkably, NMAH was also found to promote in the gas phase the U=O bond activation with the concomitant elimination of a water molecule incorporating one "yl" oxygen atom.[23]

Ligand preorganization is a well-recognized and important factor in coordination chemistry which provides an entropy-driven increase of the stability of the corresponding metal complexes. In that respect, incorporation of the binding units into small cyclic structures is an efficient means for restricting the conformational freedom of chelators with respect to open-chain analogs. This strategy has been actually adopted by several microorganisms, like *Shewanella putrefaciens* that produces putrebactin, a constrained 20-membered macrocyclic dihydroxamic acid able to stabilize VO^{3+}.[24]

Besides, in few siderophores of linear topology, such as Exochelin MN excreted by *Mycobacterium sp.*,[25-26] one of the terminal chelates is derived from 1-hydroxypiperidine-2-one or 1,2-PIPOH (hereafter abbreviated PIPOH) in which the hydroxamic acid function is part of a six-membered ring.[27] In siderophore chemistry, this subunit represents, together with the much more frequent catecholate, one instance of metal binding groups that are preorganized for chelation, as the oxygen atoms display, by construction, a *cis* orientation with respect to each other. Indeed, the cyclic scaffold of PIPOH, which adopts in the solid state a half-chair conformation owing to conjugation within the C(=O)N(OH) part, prevents the *cis* to *trans* interconversion.

Although known for more than fifty years,[28] cyclic hydroxamic acids, such as PIPOH, suffer in turn quite surprisingly from a complete lack of knowledge as far as their coordination properties are concerned. Those of PIPOH remained fully unexplored until 2015, when we reported a detailed spectroscopic and structural study of a range of tetrachelated complexes with various tetravalent metal cations of the transition (Zr, Hf), lanthanide (Ce), and actinide (Th, U) families.[27] Shortly before, we also described the very first receptor incorporating PIPO-based binding units.[29] This tetrapodal calix[4]arene derivative was shown to strongly bind zirconium(IV) and hafnium(IV) together with an additional alkaline cation (Alk = Na^+ or K^+) to form an inclusion complex of [Alk ⊂ M_2L_2] formula.

Herein, we wish to disclose a thorough physico-chemical study, in which we have compared the uranyl complexation properties of the cyclic PIPO$^-$ ligand in aqueous solution to those of the linear NMA$^-$ ligand. The major aim of this work was to quantify the stability gain brought by the blocked *cis* arrangement of the hydroxamate oxygen donor atoms found in PIPO$^-$ with respect to NMA$^-$. To that end, we have examined the complexation thermodynamics of UO_2^{2+} by successively one and two anionic chelates by combining a range of complementary techniques (potentiometry, spectrophotometry, affinity capillary electrophoresis, NMR and Raman spectroscopies). In addition, single crystals of the complex $[UO_2(PIPO)_2(H_2O)]$ were examined by X-ray diffraction, and the resulting structure is compared with those of related complexes described in the literature.

Results and discussion

Structural characterization in the solid state

Crystal structure of $[UO_2(PIPO)_2(H_2O)]$. Clear, light red single crystals of $[UO_2(PIPO)_2(H_2O)]$ were obtained by slow evaporation of an aqueous uranyl solution at pH 4–5 containing two equivalents of 1,2-PIPOH. Detailed information about data collection, crystallographic and refinement parameters are summarized in the ESI†. The asymmetric unit contains one neutral $[UO_2(PIPO)_2(H_2O)]$ complex. An ORTEP view of the corresponding molecular unit is displayed in Fig. 1, together with the atom labelling scheme.

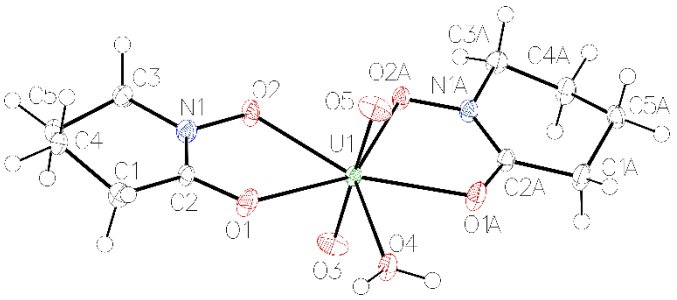

Fig. 1 ORTEP view of the $[UO_2(PIPO)_2(H_2O)]$ complex found in the asymmetric unit. Thermal ellipsoids are drawn at 50% probability level.

Similarly to the related $[UO_2(NMA)_2(H_2O)]$ compound,[15] the crystal structure of $[UO_2(PIPO)_2(H_2O)]$ shows a butterfly-like arrangement of both PIPO$^-$ ligands which are chelated in such a way that both pairs of O_C and O_N oxygen atoms are facing each

other. The bound water molecule (O4) is located in between the carbonyl oxygen atoms O1 and O1A, and interacts by a pair of hydrogen bonds with the hydroxamic O2 and O2A oxygen atoms belonging to the neighboring motif (Table S2, see ESI†), thus forming head-to-head linear chains along the *a* direction of the crystal lattice. The U···U distance between two adjacent molecular units (6.472 Å) is somewhat longer compared to that found for $[UO_2(NMA)_2(H_2O)]$ (6.424 Å).

The hydrogen-bonded chain-like assembly of $[UO_2(NMA)_2(H_2O)]$ and $[UO_2(PIPO)_2(H_2O)]$ is original among the structures of uranyl bishydroxamato complexes deposited in the Cambridge Structural Database (CSD, release 5.38),[30] although formo- (FHAH),[31] aceto- (AHAH),[32] and salicyl- (SHAH)[33] hydroxamic acids (Chart 1) also form linear coordination polymers. However, in the latter cases no water molecule is involved in the assembly, since symmetry-related adjacent hexacoordinated uranyl cations (U···U = 4.346–4.465 Å) are directly interacting with a pair of monodentate carbonyl oxygen donors and two μ_2-bridging bidentate hydroxamic N–O atoms. Besides, PBA^- and $IBPHA^-$ form isolated molecular species of $[UO_2(L)S]$ general formula, where S designates a monodentate organic solvent (MeOH, EtOH, DMF, or DMSO) unable to promote intermolecular association of the complexes unlike water.[34-36]

Considering the uranyl bond metrics, the $[UO_2(PIPO)_2(H_2O)]$ structure shows U=O distances of 1.778(4) and 1.783(4) Å with O3 and O5, respectively (Table 1), which are very close to those reported for $[UO_2(NMA)_2(H_2O)]$ (1.785(3) Å on average)[15] and, more generally, fall into the typical range found for the other crystallographically characterized hydroxamato uranyl complexes (Table S3, see ESI†). As far as the O=U=O angle is concerned (179.2(2)°), the triatomic coordination center can be considered as essentially linear, in accordance with the angular values compiled in Table S3 for the related structures. Indeed, deviations from 180° are typically less than 3.5°, with the noticeable exception of $\{[UO_2(FHA)_2]\}_n$ in which the UO_2^{2+} cation is more bent (173.5(4)°).[31]

Likewise to $[UO_2(NMA)_2(H_2O)]$, the coordination polyhedron of $[UO_2(PIPO)_2(H_2O)]$ consists of five oxygen donor atoms located in the equatorial plane, the environments around the uranyl cation being ascribed to a Johnson pentagonal bipyramid J_{13} of D_{5h} ideal point-group symmetry. Distortion from the perfect structure is reflected by slight departures from the theoretical 90° value of the O_{eq}–U–O_{yl} angles between equatorial and apical "yl" oxygen atoms (Table 1). Evidence for the near-planar arrangement of the five O1, O2, O1A, O2A, and O4 atoms is provided by the individual deviations from the corresponding least-squares plane (–0.034(3), 0.089(3), 0.097(3), –0.116(3), and –0.035(3) Å for O1, O2, O1A, O2A, and O4, respectively), while the U1 atom lies by –0.025(2) Å out of the plane. Another informative parameter measuring the planar arrangement of the donor atoms, and thus the lack of steric/electronic repulsions in the equatorial mean plane, is the sum (Σ_{eq}) of the five O_{eq}–U–O_{eq} angles (Table 1), which equals 360° for a strictly coplanar environment. This situation is almost achieved in $[UO_2(PIPO)_2(H_2O)]$, for which Σ_{eq} = 360.4(2)° (Table 1), as well as in the $[UO_2(NMA)(NO_3)(H_2O)_2]$ and $[UO_2(NMA)_2(H_2O)]$ complexes.[15] In addition, the mean O_C–U–O_N bite angle in $[UO_2(PIPO)_2(H_2O)]$ (65.8(1)°) is quite regular for uranyl hydroxamato complexes (Table S4, see ESI†) and especially very close to the values found for $[UO_2(NMA)(NO_3)(H_2O)_2]$ (64.3(1)°) and $[UO_2(NMA)_2(H_2O)]$ (64.7(1)°),[15] ruling out any kind of pincer effect imparted by the cyclohexyl scaffold of $PIPO^-$ with respect to acyclic NMA^- bidentate chelator. Moreover, the mean bite angle is also similar to that reported for $[UO_2(1,2\text{-}HOPO)_2(H_2O)]$ (66.1°), which incorporates two 1,2-hydroxypyridonate units, the aromatic counterparts of $PIPO^-$.[37]

According to the selected U–O distances summarized in Table 1, it can be concluded that both negatively charged hydroxamate oxygen atoms O2 and O2A interact somewhat less strongly with the metal than the carbonyl oxygen atoms O1 and O1A, as reflected by the average U1–O_N (2.39(1) Å) and U1–O_C distances (2.371(8) Å). As expected, the neutral water molecule forms a significantly longer U–O bond (2.424(4) Å). Overall, U–O_N and U–O_C distances conform very well to those measured for $[UO_2(NMA)_2(H_2O)]$ (U–O_N = 2.376(1)–2.402(4) Å, averaging 2.39(1) Å and U–O_C = 2.368(4)–2.387(4) Å, averaging 2.38(1) Å), although the latter complex shows a slightly shorter U–O_{water} distance of 2.367(7) Å. These results contrast with the bond metrics reported for the uranyl bis(1,2-hydroxypyridonato) complex $[UO_2(1,2\text{-}HOPO)_2(H_2O)]$, for which U–$O_N$ = 2.35(1) Å and U–O_C = 2.38(1) Å.[37]

Electronic delocalization over the O–N–C–O group of atoms accounts for their almost planar arrangement, as indicated by the close-to-zero value of the corresponding torsion angles (3.1(7)° and –2.5(7)°). As a consequence, both six-membered $PIPO^-$ rings adopt a half-chair conformation, likewise to the free PIPOH structure.[27] In terms of distances, C=O and N–O bond lengths, which average 1.310(9) and 1.351(7) Å, respectively, are clearly differentiated for $[UO_2(PIPO)_2(H_2O)]$, in agreement with the trend previously observed for the known linear[15,31-34,36,38] and aromatic[37] bishydroxamato uranyl complexes (Table S5, see ESI†). Moreover, the short C–N distances (1.308(8) Å on average) clearly reflect a partial double-bond character. Compared to the free ligand PIPOH, uranyl binding lengthens the C=O bond by 0.06 Å and shortens both the N–O and C–N distances by 0.046 and 0.02 Å, respectively, as already noticed, albeit to a slightly larger extent, for Zr^{4+}, Hf^{4+}, and U^{4+} chelation.[27]

Table 1 Selected bond lengths (Å) and angles (°) for $[UO_2(PIPO)_2(H_2O)]$

U1–O1	2.365(4)	U1–O1A	2.376(4)
U1–O2	2.384(4)	U1–O2A	2.398(3)
U1=O3	1.778(4)	U1=O5	1.783(4)
U1–O4	2.424(4)		
O1-U1-O2	66.1(1)	O1A-U1-O4	77.3(1)
O2-U1-O2A	76.5(1)	O1-U1-O4	75.0(1)
O1A-U1-O2A	65.5(1)		

Vibrational spectroscopy. X-ray quality crystals of $[UO_2(NMA)(NO_3)(H_2O)_2]$,[15] $[UO_2(NMA)_2(H_2O)]$,[15] and

$[UO_2(PIPO)_2(H_2O)]$ were characterized by FTIR and Raman spectroscopies (Figures S5–S13, see ESI†), confirming the presence of bound water molecules and of a nitrate anion in the former compound (ν_s(N–O) = 1042 cm^{-1} vs. 1050 cm^{-1} for unbound NO_3^- in KNO_3 or $[UO_2(NO_3)_2(H_2O)_2]\cdot 4H_2O$).

The naked uranyl dication of $D_{\infty h}$ point-group symmetry displays symmetric (ν_{sym}) and antisymmetric (ν_{asym}) U=O stretching modes, which are Raman and infrared active, respectively.[39] Taken as a reference, crystalline hexacoordinated uranium nitrate $[UO_2(NO_3)_2(H_2O)_2]\cdot 4H_2O$ displays a Raman shift at 869 cm^{-1} and an IR absorption band at 941 cm^{-1} (ν_{asym}) flanked by a very weak feature at 868 cm^{-1} assigned to the IR-forbidden symmetric mode. In comparison, Raman spectra collected for X-ray quality crystals of $[UO_2(NMA)(NO_3)(H_2O)_2]$, $[UO_2(NMA)_2(H_2O)]$, and $[UO_2(PIPO)_2(H_2O)]$ show intense signals assigned to the ν_s stretch of UO_2^{2+} at 858, 828, and 835 cm^{-1}, respectively. The associated antisymmetric absorption bands appear at 934, 897, and 906 cm^{-1} in the corresponding ATR-FTIR spectra. These data are in excellent agreement with values reported for $[UO_2(PBA)(THF)_2Cl]$ (ν_{sym} = 873 cm^{-1} and ν_{asym} = 934 cm^{-1}),[40] $\{[UO_2(FHA)_2]\}_n$ (ν_{sym} = 827 cm^{-1}),[31] $[UO_2(PBA)_2DMSO]$ (ν_{asym} = 910 cm^{-1}),[35] $[UO_2(PBA)_2DMF]$ (ν_{asym} = 895 cm^{-1}).[36] Uranyl chelation in the equatorial plane significantly lowers the oscillator strength and weakens the U=O bond order as the electron-donating ability of the ligands increases. As a consequence, a monotonous variation of the ν_{sym} and ν_{asym} vibrational frequencies with the U=O bond lengths is anticipated. Using the empirical expression parametrized by Bartlett and Cooney, d(U=O) = $a\ \nu^{-2/3} + b$ with a = 10650, b = 57.5 for ν_{sym} (Raman), and a = 9141, b = 80.4 for ν_{asym} (IR),[41] the consistency of our crystallographic, Raman, and IR data can be ascertained. Predicted d(U=O) distances compare favorably well with those determined by X-ray diffractometry, as the deviations are within ± 0.025 Å for the three complexes. Most importantly, the predicting power of the equation is sufficient for discriminating by vibrational spectroscopy the mono- from the bishydroxamato environnement in the crystal state.

One can therefore safely rely on the bathochromic shifts undergone by the U=O vibration mode upon binding of one ($\Delta\nu$ = 12 cm^{-1}) and two ($\Delta\nu$ = 35–42 cm^{-1}) hydroxamate anions in the solid state as a benchmark for identifying the various species occurring in aqueous solutions at a given pH (vide infra).

Electronic spectroscopy. To get a deeper insight into the electronic absorption properties, diffuse reflectance spectroscopic measurements of solid samples were undertaken either in their pure form or once ground with $BaSO_4$. Most uranium(VI) compounds, including for example the pristine uranyl nitrate, perchlorate, or acetate salts, are typically lemon-yellow owing to ligand-to-metal charge transfer bands (LMCT) of weak intensity. Albeit all visible $\sigma_u^+(2p_O) \rightarrow \delta_u(^5f_{xyz}, {}^5f_{z(x^2-y^2)})$ and $\sigma_u^+(2p_O) \rightarrow \phi_u(^5f_{y(3x^2-y^2)}, {}^5f_{x(x^2-3y^2)})$ transitions involving the "yl" oxygen and the uranium atoms are formally parity-forbidden for bare uranyl according to the Laporte selection rule, they become allowed through interactions with equatorial donor atoms provided the point group is noncentrosymmetric (static ligand field) and in any case via vibronic coupling (dynamic ligand field). Hence, the spectrum of microcrystalline $[UO_2(NO_3)_2(H_2O)_2]\cdot 4H_2O$ diluted in amorphous $BaSO_4$ shows a vibronically-resolved manifold with maxima at 385, 394, 405, 416, 428, 438, 451, 469, and 486 nm, as found in aqueous solutions for $[UO_2(H_2O)_5]^{2+}$ ($\varepsilon \sim 9.2$ M^{-1} cm^{-1}).

In contrast to inorganic uranyl salts, isolated hydroxamato complexes are all characterized by an orange-red color. The microcrystalline bischelated $[UO_2(L)_2(H_2O)]$ complexes (L = NMA$^-$ and PIPO$^-$) give rise to two broad unstructured absorption bands in the visible range centered at 386 and 501 nm for the latter (Figure S4, see ESI†). Relying on TD-DFT calculations, these features have been assigned to LMCT bands between the filled ligand-centered π and the empty uranium 5f orbitals,[31] while the UV band observed at 252 nm for the pure complex or at 226 nm once diluted in a $BaSO_4$ matrix corresponds likely to $\pi \rightarrow \pi^*$ transitions within the hydroxamate anions, as found also for the free ligand. Likewise, the diffuse reflectance spectrum of the red-colored $\{[UO_2(FHA)_2]\}_n$ coordination polymer shows two bands at ~ 370 and 475 nm. Silver et al. tentatively explained the occurrence of these two LMCT bands by the distortion experienced by the UO_2^{2+} cation as the O=U=O angle reaches 173° (Table S3, see ESI†)[31] Obviously, this explanation cannot withstand the present findings, as our complexes give rise to very similar electronic spectra in the solid state, with much more linear uranyl cations. At best, the UO_2^{2+} bending can account for slight variations in the transition energies and probabilities. The orange-red color associated to both LMCT bands is a common feature among uranyl mono- and bishydroxamato complexes both in the solid state as well as in solution (vide infra).[34-36,40,42-46]

Ligand protonation equilibria

Potentiometry. The protonation constants at 298.2(1) K of the conjugated bases NMA$^-$ and PIPO$^-$ have been measured in triplicates by glass-electrode potentiometry in 0.1 M KNO_3 solutions (black curve in Fig. 2). Forward and backward titration curves do not show any hysteresis effect over the explored p[H] region 2–11, in which both ligands behave, as expected, as moderately weak monoprotonic bases (Table 2).

Table 2 Thermodynamic parameters for the protonation and uranyl complex formation equilibria involving NMA$^-$ and PIPO$^-$ in aqueous media [a]

Equilibrium		NMA$^-$	PIPO$^-$
$L^- + H^+ \leftrightarrows LH$	log K_{011}	8.68(3)[b]	8.85(2)[b]
	$\Delta_r G_{011}$ (kJ mol^{-1})	–49.5(2)[b]	–50.5(1)[b]
	$\Delta_r H_{011}$ (kJ mol^{-1})	–12.7(2)[c]	–19.3(1)[c]
	$-T\Delta_r S_{011}$ (kJ mol^{-1})	–36.8(3)	–31.2(2)
$UO_2^{2+} + L^- \leftrightarrows [UO_2(L)]^+$	log K_{110}	7.76(1)[b]	8.58(1)[b]
		7.81(1)[d]	8.58(1)[d]
		n. d.	8.60(5)[e]
$[UO_2(L)]^+ + L^- \leftrightarrows [UO_2(L)_2]$	log K_{120}	6.14(1)[b]	6.92(1)[b]
		6.47(1)[d]	7.00(1)[d]

[a] I = 0.1 M KNO_3, T = 298.2(1) K unless otherwise noted. [b] Glass-electrode potentiometry. [c] Isothermal titration calorimetry. [d] Spectrophotometry. [e] Affinity capillary electrophoresis. I = 0.1 M (H,Na)ClO_4, T = 298.2(5) K. n. d.: not determined.

The log K_{011} value determined herein for NMA^- (8.68(3)) supports earlier findings for similar conditions (literature values are compiled in Table S7, see ESI†), and falls in the typical range found for hydroxamates (8.5–9.4). Obviously, the overall basicity is modulated by the substitution pattern, especially by the nature of the R^2 motif attached to the nitrogen atom, whereas the effect of the carbonyl substituent R^1 should be less pronounced.[47] Owing to the electron-donating effect of a methyl group, NMA^- would be expected at first sight to be more basic than AHA^-. This anion is also expected to be better solvated than the *N*-methyl derivative, as the N–H fragment is likely involved in hydrogen bonding with surrounding water molecules, stabilizing the AHA^- anion and making it *a priori* more difficult to protonate. In fact, it turns out that AHA^- is significantly more basic (log K_{011} = 9.30(4) at I = 0.1 M)[48-49] than NMA^-. To understand why the reverse situation is encountered, the electron delocalization scheme of hydroxamates has to be considered (Chart 2).

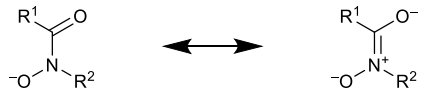

Chart 2 Resonance structures of hydroxamate anions

A positive charge builds up on the nitrogen atom in the iminium resonance form, which is stabilized either by a positive inductive effect of the *N*-methyl group in case of NMA^- or by additional resonance with the *N*-phenyl ring for NPA^- (log K_{011} = 8.47 at I = 0.2 M KCl).[48] As this canonical form in the resonance scheme gains more and more weight for R^2 = H, Me, and Ph, the corresponding anions are increasingly stabilized in the order $AHA^- < NMA^- < NPA^-$, and their basicity lowered in the opposite order.

To rationalize the slightly stronger basicity of $PIPO^-$ (log K_{011} = 8.85(2)) compared to that of NMA^- (log K_{011} = 8.68(3)), an additional factor should be considered. As stressed in the introduction, the latter exists in aqueous solution as a mixture of two rotamers in equilibrium owing to the restricted rotation around the C–N bond, which can be again understood by the resonance scheme depicted in Chart 2. Both NMA^- and NMAH prevail in their *E* form, but not in the same ratio with the *Z* one (9.63 and 2.86, respectively), so as to minimize repulsive electronic interactions between the oxygen atoms.[15-16,18] By contrast, $PIPO^-$ is blocked in the *Z* conformation by construction, and thus is unable to alleviate these electrostatic interactions by a conformational change. This destabilization results in a relatively higher proton affinity by comparison to NMA^-. However, the stronger electron donating effect of the tetramethylenic chain with respect to a methyl group should contribute to stabilize more the iminium resonance form of $PIPO^-$ than that of NMA^-. Both effects having opposite consequences on the ligand basicity, almost cancel each other, as the net $\Delta\Delta G_{011}$ amounts only 1 kJ mol^{-1} in favour of the cyclic hydroxamate. The fact that $PIPO^-$ is a slightly stronger base than the acyclic NMA^- unit and, to an ever greater extent, other aromatic analogues, such as 1-hydroxy-2-pyridonate (1,2-$HOPO^-$, log K_{011} = 5.86 for I = 0.1 M, T = 298.2 K)[49] and 3-hydroxy-2-methyl-3H-quinazolin-4-one (Cha^-, log K_{011} = 6.05 for I = 0.2 M KCl, T = 298.2 K),[50] makes this compound an interesting chelator for Lewis-acidic metals, including the uranyl dication.

Isothermal titration calorimetry (ITC). Protonation enthalpies ($\Delta_r H_{011}$) determined in 0.1 M KNO_3 at 298.15(1) K by ITC for NMA^- and $PIPO^-$ are gathered in Table 2, together with the Gibbs free enthalpy changes ($\Delta_r G_{011} = -RT \ln K_{011}$) and the entropic terms $-T\Delta_r S_{011}$, while a representative thermogram can be found in the ESI† (Figures S15–S16). The presented ITC data for NMA^- are in qualitative agreement with those reported by Fazary ($\Delta_r H_{011}$ = –36.5 kJ mol^{-1}, $-T\Delta_r S_{011}$ = –14.4 kJ mol^{-1}, I = 0.1 M $NaNO_3$, T = 298.15 K)[51] and Monzyk and Crumbliss ($\Delta_r H_{011}$ = –5(2) kJ mol^{-1}, $-T\Delta_r S_{011}$ = 45(2) kJ mol^{-1}, I = 2 M $NaNO_3$, T = 298.15 K).[47] In both studies, reaction enthalpies and entropies were derived from a Van't Hoff plot of p*K*a's measured over a narrow temperature range (ΔT = 20 K), while the data of Monzyk and Crumbliss are also vitiated by a systematic error since the p*K*a values implicitly take into account the activity coefficients for the proton.

With respect to NMA^-, the protonation process of $PIPO^-$ is more exothermic by 6.6 kJ mol^{-1}. The measured $\Delta_r H_{011}$ values reflect the contributions for desolvating both the hydroxamate anion and proton, forming the NO–H bond, rotating the C–N bond in case of NMAH, and solvating the acid form. The more negative protonation enthalpy measured for $PIPO^-$, which assumes a blocked conformation and appears more hydrophobic than NMA^- and thus less well solvated (vide infra), confirms that the former has a higher basicity than the latter. Overall, the protonation process of both anions is mainly entropy driven as $-T\Delta_r S_{011}$ is about two times larger than $\Delta_r H_{011}$, a fact that can be easily rationalized by a net release of water molecules upon converting polar ionic species into less polar neutral ones. The entropy change for $PIPO^-$ at 298.15 K is by 5.6 kJ mol^{-1} lower than the one estimated for NMA^-, suggesting that the cyclic structure is less solvated as might be expected when two methyl groups are replaced by an aliphatic C_4 chain. However, an additional factor has to be considered, namely the shift of the *E*/*Z* equilibrium undergone upon protonation of NMA^-, which is also expected to contribute to the larger entropic change.

UO_2^{2+} complexation equilibria

Potentiometry. For each ligand, the uranyl speciation as a function of p[H] has been investigated at first by glass-electrode potentiometry at constant ionic strength (I = 0.1 M KNO_3) and temperature (T = 298.2(2) K). Representative titration curves for 1:1 and 1:2 total uranyl/NMA^- concentration ratios are shown in Fig. 2 (experiments were duplicated for each ratio), together with the neutralization curve collected for NMAH alone. The UO_2^{2+}/$PIPO^-$ system behaves essentially in the same way.

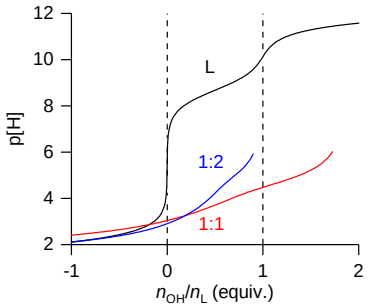

Fig. 2 Potentiometric titration of the UO_2^{2+}/NMAH system as a function of p[H]. I = 0.1 M KNO_3, T = 298.2(1) K.

In all experiments, the p[H] was raised up to ~ 5.5, corresponding to the precipitation onset. A deep orange-red solid was recovered by filtration, ruling out the formation of yellow uranyl hydroxide. To confirm the identity of the recovered solid, the experiment was repeated on a preparative scale without adding KNO_3 as supporting electrolyte. For both ligands, the recovered material once dried turned out to be microcrystalline, thus enabling to record X-ray powder diffraction patterns (Figures S1–S3, see ESI†) which compare favorably well with the theoretical diffractograms computed from the single-crystal structures of the $[UO_2(L)_2(H_2O)]$ complexes. Further evidence for the precipitation of the neutral bischelate was provided by spectroscopic investigations (IR, Raman, diffuse reflectance in the visible range (Figures S4, S7, S9, and S14 in ESI†) and absorption spectrophotometry after dissolution in diluted HNO_3). By increasing the p[H] above neutrality, the solid only partially dissolved suggesting the formation of additional hydrolyzed species, most likely the anionic $[UO_2(L)_2(OH)]^-$ complex that could only be characterized by Raman spectroscopy (Figure S12, see ESI†).

Since precipitates of $[UO_2(L)_2(H_2O)]$ were unfortunately always present in the p[H] range 5.5–10.9, no accurate stability constants for the anionic monohydroxo species (β_{12-1}) could be measured. Hence, only titration data collected in the acidic conditions (p[H] < 5.5) were processed by nonlinear least-squares with the Hyperquad 2013 program to extract the overall equilibrium constants for complex formation defined by eqn (1) and (2).[52] During the simultaneous refinement of all titration curves, the known values of the protonation constant (β_{011}) of the ligands (Table 2) and of the hydrolysis constants of uranyl (β_{m0-h}) taken from the literature (Table S8, see ESI†) were treated as fixed parameters. [53-54]

$$m\,UO_2^{2+} + l\,L^- + h\,H^+ \leftrightarrows [(UO_2)_m(L)_lH_h]^{(2m+h-l)+}$$
$$m\,UO_2^{2+} + l\,L^- + h\,H_2O \leftrightarrows [(UO_2)_m(L)_l(OH)_h]^{(l+h-2m)-} + h\,H^+ \quad (1)$$

$$\beta_{mlh} = \frac{[(UO_2)_m(L)_lH_h]}{[UO_2]^m[L]^l[H]^h}$$
$$\beta_{ml-h} = \frac{[(UO_2)_m(L)_l(OH)_h][H]^h}{[UO_2]^m[L]^l} \quad (2)$$

The best fit was obtained with a model including the formation of both a single (β_{110}) and a bischelated (β_{120}) complex, while the trischelate species (β_{130}) and hydroxo complexes (β_{12-h}) were systematically rejected. Logarithmic values reported in Table 2 correspond to the stepwise binding constants defined as $K_{110} = \beta_{110}$ and $K_{120} = \beta_{120}/\beta_{110}$. Binding constants found for NMA^- lie in between those reported at the same temperature and ionic strength for AHA^- (log K_{110} = 8.22, log K_{120} = 7.08) or BHA^- (log K_{110} = 7.49, log K_{120} = 6.68).[49]

Noteworthy, mono- and bischelate complexes formed with $PIPO^-$ are by 0.80(2) logarithmic units more stable than those with NMA^-. The enhanced affinity of $PIPO^-$ for UO_2^{2+} and $[UO_2(PIPO)(H_2O)_3]^+$, which amounts to 4.6 kJ mol^{-1} in both cases, can be explained both by its slightly higher basicity (enthalpic factor) and by the preorganization of both oxygen donor atoms locked in the favorable *cis* conformation (entropic factor). Conversely, NMA^- prevails at 90.6% as the *trans* or *E* rotamer in aqueous solution (K_{ZE} = 9.63(5) at 300 K).[15] Therefore, the major fraction needs to undergo an energetically unfavorable *trans* to *cis* interconversion (rotation around the C–N bond) prior to the chelate ring closure. The free-energy cost for this rearrangement (0.906 × $\Delta G_{E\to Z}$ = 5.1 kJ mol^{-1}), as determined for NMA^- by NMR spectroscopy in an earlier work,[15] is very close to the aforementioned stability difference.

As encountered for the vast majority of systems, the stepwise binding constants decrease steadily as the number of coordinated ligands increases, a phenomenon classically refereed to non-cooperativity. It is however remarkable to note an identical difference between log K_{110} and log K_{120} for each considered ligand ($\Delta_{1,2}$ = log K_{110} – log K_{120} = 1.62 for NMA^- vs. 1.66 for $PIPO^-$). Generally speaking, statistical, steric, solvation, and electronic effects are the main factors accounting for the gradual decrease in affinity ($\Delta\Delta G_{1,2}$ = 9.2 vs. 9.4 kJ mol^{-1} for NMA^- and $PIPO^-$, respectively).

The first effect, which reflects the decreasing probability of an entering bidentate chelator to find an unoccupied binding position, can be easily factored out by assuming a pentacoordinated uranium center in the equatorial plane, as revealed by the crystal structures. For the first and second binding events, there are 10 and 4 possibilities to arrange an unsymmetrical bidentate ligand along one of the five equivalent edges of a pentagon, respectively. Likewise, there are 1 and 2 ways to dissociate one bound ligand from ML and ML_2. Hence, in the case of purely statistical binding, the macroscopic binding constants are expected to decrease in the order $^{10}/_1\,Q < {}^4/_2\,Q$, where Q is the intrinsic or site-specific microscopic binding constant.[55-56] It follows that K_{110} and K_{120} should be in the ratio 5/1. In other words, log K_{120} is expected to be lowered by 0.70 unit with respect to log K_{110} ($\Delta\Delta G_{stat}$ = 4.0 kJ mol^{-1}).

Experimentally, the $\Delta_{1,2}$ difference is slightly more than twice larger than the statistical factor of 0.70, suggesting that the steric and electrostatic contributions to the stability decrease should amount ca. 5 kJ mol^{-1}. From a simple visual inspection of both $[UO_2(NMA)_2(H_2O)]$[15] and $[UO_2(PIPO)_2(H_2O)]$ crystal structures (Fig. 1) or a more detailed analysis of the coordination spheres, it can be safely concluded that the interligand interaction energy caused by steric crowding is most likely negligible. Thus, the lower stability of $[UO_2(L)_2(H_2O)]$ with respect to $[UO_2(L)(H_2O)_3]^+$ should mainly be related to the lower

electrostatic interaction energy resulting from the overall charge reduction on uranyl upon uptake of the second hydroxamate anion.

Visible absorption spectrophotometry. Owing to the characteristic orange-red color of the uranyl complexes with hydroxamate ligands, the speciation model was further ascertained by monitoring the p[H] titrations of solutions containing a two-fold ligand excess by visible absorption spectrotophotometry. A representative set of spectra collected in the 350–650 nm range is displayed in Fig. 3a. Upon increasing the p[H] from 2 up to about 5.5, two visible absorption bands centered around 390 and 487 nm progressively gain in intensity. The maximum of the high-energy band undergoes a slight hypsochromic shift (λ_{max} = 381 nm), while the transition energy associated with the second component remains unchanged. Factor analysis clearly confirmed that no more than three absorbing species account for the spectral changes above the noise level. The simultaneous multiwavelength processing of all data sets by the nonlinear least-squares refinement program Hyperquad 2006, which solves the mass balance equations for the metal, ligand, and the proton,[52] returned equilibrium constants that are in excellent agreement with those measured by potentiometry alone (Table 2).

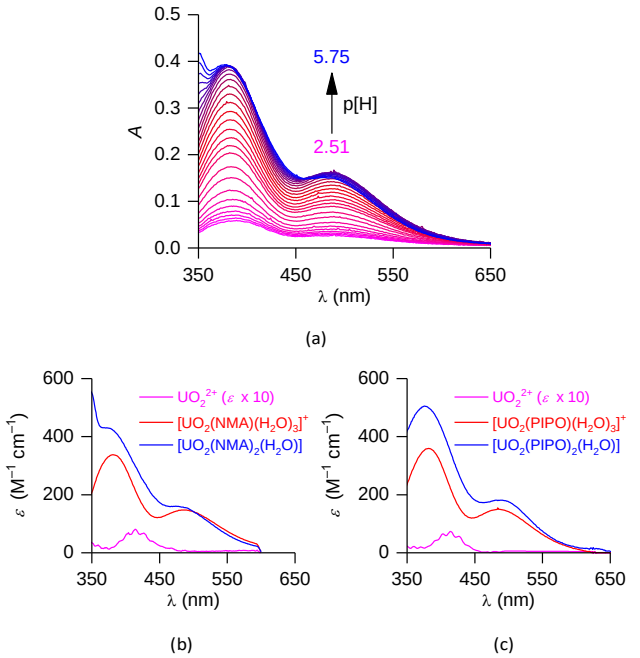

Fig. 3 (a) Spectrophotometric titration of the UO_2^{2+}/NMAH system as a function of p[H]. I = 0.1 M KNO_3, T = 298.2(1) K, $[U(VI)]_{tot}$ = 1.35 mM, $[NMAH]_{tot}$ = 2.97 mM, l = 1 cm. (b) Calculated electronic spectra for the UO_2^{2+}/NMAH (b) and UO_2^{2+}/PIPOH (c) systems.

The calculated electronic spectra are reproduced in Fig. 3b (NMA^-) and Fig. 3c ($PIPO^-$). For both ligands, the monochelated species are characterized by two absorption maxima at λ_{max} = 382 nm (ε = 338 and 360 M^{-1} cm^{-1} for NMA^- and $PIPO^-$, respectively) and λ_{max} = 486 nm (ε = 147 and 150 M^{-1} cm^{-1} for NMA^- and $PIPO^-$, respectively). Upon chelation of a second hydroxamate anion, the first band undergoes a slight hypsochromic (λ_{max} = 375 nm) and a hyperchromic shift (ε = 430 and 505 M^{-1} cm^{-1} for NMA^- and $PIPO^-$, respectively), while the low-energy band remains almost unaffected: λ_{max} = 475 nm (ε = 160 M^{-1} cm^{-1}) for NMA^- and λ_{max} = 487 nm (ε = 180 M^{-1} cm^{-1}) for $PIPO^-$, respectively. Although both CT bands occur at slightly lower wavelengths in solution with respect to the solid state (Figure S4, see ESI†), the close resemblance with the diffuse reflectance spectrum suggests that the structure found in the crystal is retained upon dissolution. Moreover, a reasonable absorption spectrum for the very-weakly absorbing free uranyl cation could be calculated for the UO_2^{2+}/NMAH system, which reproduces quite well the vibronic fine structure with a maximum at 414 nm (ε = 8.1 M^{-1} cm^{-1}). In turn, this spectrum had to be fixed for the UO_2^{2+}/PIPOH system to let the refinement converge.

Raman spectroscopy. Owing to the high sensitivity of the symmetrical O=U=O bond stretch (ν_{sym}) to the equatorial ligand field strength, uranyl complex formation equilibria in 0.1 M KNO_3 with NMA^- and $PIPO^-$ have also been monitored by Raman spectroscopy as a function of p[H] (Fig. 4). In a typical titration, a two or four-fold excess of chelator over the total uranyl concentration was used ($[U(VI)]_{tot}$ = 20–25 mM). All spectra were normalized with respect to the ν_{sym} stretch of the free nitrate anion appearing at 1048 cm^{-1}.[39]

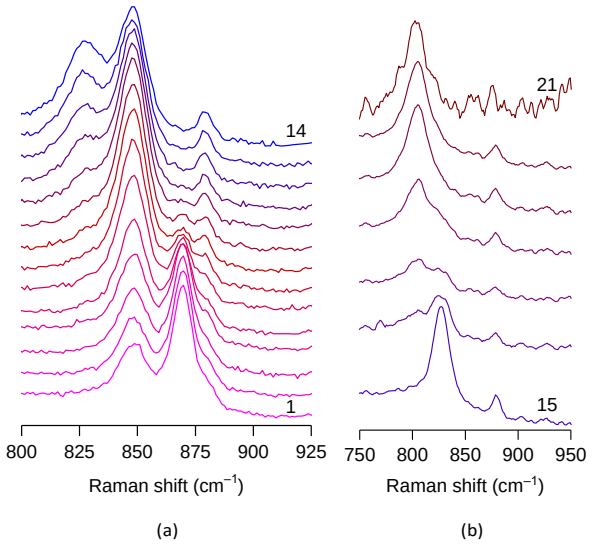

Fig. 4 Raman spectra collected as a function of p[H] for the UO_2^{2+}/$PIPO^-$ system. I = 0.1 M KNO_3, T = 298.2(2) K. (a) $[U(VI)]_{tot}$ = 25.1 mM, $[PIPOH]_{tot}$ = 50.3 mM, p[H] (spectra 1–14): 1.17, 1.20, 1.33, 1.47, 1.68, 2.01, 2.24, 2.55, 2.80, 3.09, 3.42, 3.63, 3.87, 4.04. (b) $[U(VI)]_{tot}$ = 20 mM, $[PIPOH]_{tot}$ = 60 mM, p[H] (spectra 15–21): 5.74, 6.88, 7.54, 7.85, 8.74, 9.77, 10.92.

In the 800–900 cm^{-1} range, the spectra are dominated at low p[H] by a band centered at 869 cm^{-1} that is readily assigned to the uranyl aqua ion $[UO_2(H_2O)_5]^{2+}$ (Fig. 4a).[39,57] Upon raising the p[H], this feature tends to progressively disappear and completely vanishes around p[H] 3. Simultaneously, a new band of increasing intensity appears at 848 cm^{-1}, which can be attributed to the formation of the monochelated $[UO_2(L)(H_2O)_3]^+$ species. This vibration frequency is blue shifted by 10 cm^{-1} with respect to the value determined for $[UO_2(NMA)(NO_3)(H_2O)_2]$ single crystals (ν_{sym} = 858 cm^{-1}).[15] This

difference suggests that a water molecule is a stronger σ-donor than a monodentate nitrate anion, in agreement with the shorter crystallographic U–OH_2 bond lengths (2.39 Å on average) compared to the U–ONO_2 distance (2.474 Å).[15]

Above p[H] ~ 2.5, the 848 cm^{-1} band is progressively replaced by another vibration mode that grows at 831 cm^{-1} (Fig. 4a). This feature can be unambiguously assigned to the bischelated complex considering the similarity of the vibration energies in solution and for single-crystals of $[UO_2(NMA)_2(H_2O)]$ (828 cm^{-1})[15] and $[UO_2(PIPO)_2(H_2O)]$ (835 cm^{-1}). In the p[H] range 6–7, precipitation of the neutral complexes prevented to record good quality spectra (Fig. 4b). However, partial re-dissolution occurring in more basic conditions allowed us to recover a signal of increasing intensity at 805 cm^{-1}, while the solution color was progressively shifting from red to orange. These changes support the deprotonation of the bound water molecule, yielding the negatively charged monohydroxo complexes $[UO_2(L)_2(OH)]^-$. Above p[H] ~ 10.9, samples became light yellow and severely cloudy with a marked drop in the signal/noise ratio caused by complex dissociation and precipitation of $UO_2(OH)_2$.

The bathochromic shifts of 21 and 17 cm^{-1} experienced by the uranyl Raman mode upon binding a first and then a second bidentate NMA^- or $PIPO^-$ anions is almost identical to the one observed for the displacement of the equatorial water molecule by OH^- ($\Delta\nu_{sym}$ = 26 cm^{-1}). This incremental variation follows quite well the empirical linear correlation (eqn (3)) between the ν_{sym} Raman shift and the equatorial coordination number of uranyl, which has been parametrized by Nguyen-Trung et al. for various ligands (CO_3^{2-}, Cl^-, OH^-…).[58]

$$\tilde{\nu}_{sym} = 870 - An \qquad (3)$$

In eqn (3), the Raman vibration frequency for a given complex containing *n* equatorial ligands is obtained by subtracting a constant increment *An* (*A* = 21.5 cm^{-1} in case of OH^-) from the characteristic wavenumber found for $[UO_2(H_2O)_5]^{2+}$ (870 cm^{-1}). The slope of 21.5 cm^{-1} reported by these authors for the $[(UO_2)_m(OH)_h]^{2m-h}$ uranyl hydroxo species is in very good agreement with the shift of 26 cm^{-1} found herein for the hydrolysis of the $[UO_2(L)_2(H_2O)]$ complexes with both hydroxamates. Moreover, the same factor enables to reliably predict the wavenumber change induced by the bidentate chelation of a monoanionic hydroxamate motif. It can therefore be concluded that both OH^- and hydroxamate ligands bind to uranyl with a similar σ-bond strength.

Besides providing structural information about the chemical environment in the equatorial plane of the uranyl center, we checked the capabilities of Raman spectroscopy as a quantitative speciation tool. For that purpose, all the collected spectra were deconvoluted by fitting the bands assigned to the unbound metal and the two $[UO_2(L)(H_2O)_3]^+$ and $[UO_2(L)_2(H_2O)]$ complexes with Lorentzian functions. The corresponding molar fractions were deduced from the relative area of each spectral component, assuming that no other minor species, such as uranyl hydrolysis products or weak nitrato complexes, were present in significant amount. This assumption is well supported by the distribution diagrams shown in Fig. 5 for both ligand systems. Formation curves, calculated with the equilibrium constants obtained by potentiometry (Table 2 and Table S8, see ESI†), reproduce quite well the overlaid Raman data that have been collected at 10-fold higher overall concentration levels compared to those employed for spectro-potentiometric measurements. This good match confirms the accuracy of our speciation model and reliability of Raman line-shape analysis for predicting the uranyl speciation in homogeneous media.

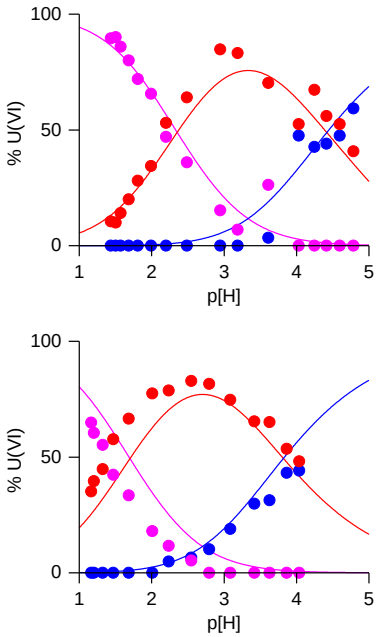

Fig. 5 Distribution diagrams for the UO_2^{2+}/NMA^- (top) and $PIPO^-$ (bottom) systems corresponding to the Raman titration conditions. Formation curves drawn as solid lines were computed with the equilibrium constants retrieved from the potentiometric model. The molar fraction of each species deduced from the Lorentzian band shape analysis of the Raman spectra are represented by filled circles. $[U(VI)]_{tot}$ = 25 mM, $[LH]_{tot}$ = 50 mM, $[KNO_3]$ = 0.1 M, *T* = 298.2(5) K. Color code: UO_2^{2+} (magenta), $[UO_2(L)(H_2O)_3]^+$ (red), $[UO_2(L)_2(H_2O)]$ (blue).

Affinity capillary electrophoresis. In the last years, affinity capillary electrophoresis (ACE) has been successfully used for studying chemical equilibria in solution and for determining stability constants of metal complexes, including actinides.[59-66] As this method allows to investigate the speciation of a cation in the presence of very large excesses of ligand, it was used to further ascertain the binding model and to detect the potential formation of trischelated species. To that end, electrophoregrams for the UO_2^{2+}/PIPOH system have been recorded for 0.1 mM uranyl solutions injected into the background electrolyte (BGE, 0.1 M (H,Na)ClO_4) containing up to 500 equiv. of ligand ($[PIPOH]_{tot}$ = 0.5–50 mM). To prevent hydrolysis of uranyl, the p[H] was maintained at 2.50(5) with perchloric acid.

A single peak of growing intensity was detected by UV spectroscopy at 250 nm, while at 200 nm the peak area was steadily decreasing. However, at both wavelengths, the UV signal shifted towards longer migration times with increasing ligand concentrations (Figure S17, see ESI†), suggesting a decrease in mobility of the labile species under observation.[67]

The sigmoidal variation of the experimental electrophoretic mobility of uranyl as a function of the total PIPOH concentration is depicted in Fig. 6.

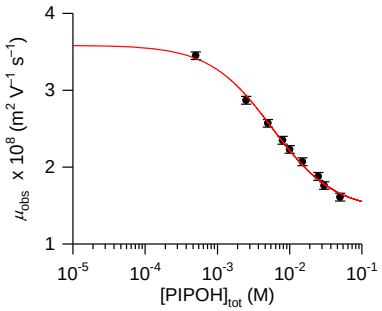

Fig. 6 Variations of the observed electrophoretic mobility of uranyl as a function of the total PIPOH concentration. I = 0.1 M (H,Na)ClO_4, T = 298.2(5) K, p[H] = 2.50(5), $[U(VI)]_{tot}$ = 0.1 mM. The red line corresponds to the best fit obtained for the UO_2^{2+} + PIPOH ⇆ $[UO_2(PIPO)]^+$ + H^+ equilibrium.

Since the time required to reach equilibrium is much faster than the separation time, the observed electrophoretic mobility of uranyl (μ_{obs}) equals the weighted sum of the mobility of each charged metallic species, as expressed by eqn (4), where α_{mlh} stands for the molar fraction and μ_{mlh} for the intrinsic electrophoretic mobility of the pure species.

$$\mu_{\text{obs}} = \sum \alpha_{mlh}\, \mu_{mlh} \qquad (4)$$

Eqn (4) is homogeneous to the expression of the NMR chemical shift for a given spin system present in several species in fast exchange. Thus, ACE data can be advantageously processed with the HypNMR program to determine simultaneously by nonlinear least-squares both the equilibrium constants and the individual electrophoretic mobilities (μ_{mlh}), while solving the mass-balance equations for each data point.[68] The best fit (red line in Fig. 6) was obtained for a single equilibrium model involving the sole formation of the $[UO_2(PIPO)(H_2O)_3]^+$ complex (eqn. (5), water molecules omitted) over the entire concentration range.

$$UO_2^{2+} + \text{PIPOH} \leftrightarrows [UO_2(PIPO)]^+ + H^+ \qquad (5)$$

The refined conditional equilibrium constant at p[H] = 2.5, as defined by eqn (6), is log K^*_{110} = 2.25(5).

$$\log K^*_{110} = \frac{[UO_2(PIPO)][H]}{[UO_2][PIPOH]} \qquad (6)$$

Taking into account the protonation state of the ligand at p[H] = 2.5, the overall stability constant given by eqn (7) is log β_{110} = 8.60(5), which agrees very well with the values measured by potentiometry and spectrophotometry (Table 2).

$$\log \beta_{110} = \log K^*_{110} + \log(1 + \beta_{011}\,[H]) \qquad (7)$$

In these conditions, the calculated mobility for free UO_2^{2+} (μ_{100} = 3.59(6) × 10^{-8} m^2 V^{-1} s^{-1}) is consistent with the experimental value (μ_{100} = 3.49(5) × 10^{-8} m^2 V^{-1} s^{-1}) deduced from the migration time observed in the absence of chelator. Owing to its lower overall electric charge and larger hydrodynamic radius, $[UO_2(PIPO)(H_2O)_3]^+$ possesses as expected a ca. 2.5-fold lower intrinsic electrophoretic mobility (μ_{110} = 1.44(6) × 10^{-8} m^2 V^{-1} s^{-1}).

Fixing the mobility of free uranyl to the experimental value during the optimization did not affect significantly the returned log K^*_{110} value (2.18(4) instead of 2.25(5)). However, the program returned unrealistically high standard deviations when the second equilibrium describing the formation of the neutral bischelated $[UO_2(PIPO)_2(H_2O)]$ species (μ_{120} = 0 m^2 V^{-1} s^{-1}) was introduced in the model. According to the distribution diagram constructed with the full set of equilibrium constants derived by potentiometry (Fig. 7), it becomes obvious that the $[UO_2(PIPO)_2(H_2O)]$ complex is a minor species under the experimental conditions used for the electrophoretic measurements. In spite of a very large excess of ligand over metal, the molar fraction of this complex does not exceed 14% at p[H] = 2.5, even at the highest considered PIPOH concentration corresponding to 500 equiv. Under such circumstances, it turns out that the contribution of the neutral bischelate to the overall mobility is too low and cannot be reliably modelled by the additional fit parameter β_{120}, considering the very large associated error.

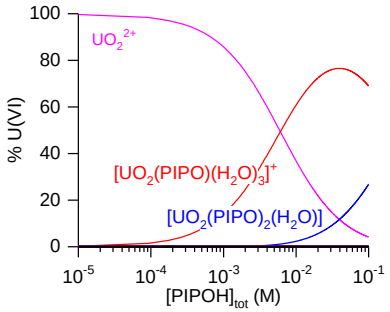

Fig. 7 Distribution diagram corresponding to the experimental conditions used to acquire the ACE data. Equilibrium constants used to compute the formation curves were taken from the potentiometric model. I = 0.1 M KNO_3, T = 298.2(2) K, p[H] = 2.5, $[U(VI)]_{tot}$ = 0.1 mM.

^{1}H NMR spectroscopy. Owing to the slow rotation around the C–N bond of NMAH, the proton NMR spectrum in D_2O shows two sets of signals for the methyl groups, which correspond to the *cis* and *trans* rotamers.[15] Upon addition of either 0.5 or 1 equiv. of uranyl to a NMAH solution at pH ~ 1.7, both singlets at 2.09 and 3.36 ppm arising from the *cis* form of the ligand are replaced at lower fields (2.33 and 3.62 ppm) by two new broad resonances owing to complex formation (Figures S18–S19, see ESI†). However, these two signals overlap with the pair of sharp singlets at 2.13 and 3.24 ppm arising from the *trans* rotamer of the unbound fraction of NMAH. Raising the pH up to ca. 5 induces a continuous downfield shift of both broad resonances assigned to the complexes and a concomitant intensity decrease in absence of any shift of the singlets arising

from *trans*-NMAH. Altogether, these observations indicate that the *cis* form of the free ligand, the mono- and bischelated uranyl complexes are in the fast exchange regime at the ^{1}H NMR timescale. It means that uranyl binding and ligand exchange takes place in a few μs or less, while the *trans* to *cis* interconversion of the free NMAH is much slower as it occurs in the 200 ms time range.[15,18]

This behavior was confirmed by ^{1}H NMR DOSY spectroscopy (Figure S20, see ESI†), which basically showed two diffusing species at 300 K besides DHO (D = 2.15(1) × 10^{-9} m^2 s^{-1} in reasonable agreement with the literature value of 1.99 × 10^{-9} m^2 s^{-1}).[69] One corresponds to the *trans* conformer of the unbound ligand (D = 8.3(2) × 10^{-10} m^2 s^{-1}) and the other one to the complexes and the *cis* conformer of NMAH in fast exchange. When the pH was raised from 3.6 to 4.8 for an equimolar mixture of NMAH and UO_2^{2+}, the mean diffusion coefficient slightly dropped from 5.77(2) to 5.46(2) × 10^{-10} m^2 s^{-1}, as expected owing to the equilibrium shift towards the formation of $[UO_2(NMA)_2(H_2O)]$ that diffuses more slowly than $[UO_2(NMA)(H_2O)_3]$. Similar observations were made for a 1:2 metal-over-ligand concentration ratio when the pH changed from 3.7 (D = 6.12(5) × 10^{-10} m^2 s^{-1}) to 5.2 (D = 5.74(1) × 10^{-10} m^2 s^{-1}).

Conclusions

The bidentate chelators *N*-methylacetohydroxamic acid (NMAH) and its 6-membered cyclic analog 1-hydroxypiperidine-2-one (PIPOH) readily form pentacoordinated uranyl complexes of $[UO_2(L)(H_2O)_3]^+$ and $[UO_2(L)_2(H_2O)]$ stoichiometry in mild acidic conditions. X-ray crystallography provided evidence for very similar structural characteristics of both bischelates with NMA^- and $PIPO^-$. Both complexes exhibit a butterfly-like arrangement of the ligands located in an essentially flat equatorial coordination plane, avoiding thereby any steric congestion between the binding motifs and the water molecule. Owing to the electron delocalization within the almost planar hydroxamate fragment, the $PIPO^-$ ring adopts a half-chair conformation. In contrast to NMA^-, which prevails in aqueous media in the *trans* or *E* form, the cyclic structure of $PIPO^-$ prevents the rotation around the C–N bond and preorganizes the *cis* or *Z* oriented oxygen donors for cation binding. As a direct consequence, $PIPO^-$ behaves as a slightly stronger base than NMA^-, the free enthalpy gain being equivalent to the energetic cost for the *trans* to *cis* interconversion paid by the latter. Overall, calorimetric investigations indicate that the protonation process of both chelators is largely entropy driven. Solution speciation studies in the presence of uranyl were undertaken over a large concentration range and metal-over-ligand concentration ratios by combining glass-electrode potentiometry, visible absorption spectrophotometry, Raman spectroscopy, and affinity capillary electrophoresis. Consistent stability constants for the mono- and bishydroxamato complexes could be determined by the four complementary methods, although partial precipitation above p[H] ~ 5 of the neutral bischelate prevented a precise estimation of the first hydrolysis constant. As expected, the preorganization of both donor atoms in the most favorable position for chelate ring formation, together with the higher basicity of $PIPO^-$, translates into a greater thermodynamic stability of the uranyl complexes. The gain over NMA^- amounts to about 0.8 order of magnitude for both the mono- and bischelated species. Raman spectroscopy turned out to be a sensitive method for probing the chemical environment around uranyl, but also for quantifying the various species in equilibrium. The frequency of the symmetrical O=U=O stretch found at 869 cm^{-1} for the pentaaquo dication in acidic solutions, is shifted to lower wavenumbers by ca. 20 cm^{-1} for each substitution of two water molecules by a bidentate hydroxamato ligand, while formation of the hydroxo complex $[UO_2(L)_2(OH)]^-$ was ascertained by an additional shift of similar amplitude, with a band appearing at 805 cm^{-1}. Finally, ^{1}H NMR studies with NMA^- confirmed the fast binding and ligand-exchange kinetics at the μs time-scale.

Overall, these results pave the way towards a better understanding of the chelation properties of hydroxamic siderophores, as NMA^- and $PIPO^-$ can be considered as structural models for their binding units. Thus far, the impact of these ubiquitous microbial chelators in soils on the migration and solubilization of uranium-rich minerals is only poorly understood but is relevant with respect to the long-term storage of nuclear wastes in geological repositories or the management of contaminated fields and mining areas. Further work in that direction is pursued.

Experimental

Safety note

Uranium (primary isotope ^{238}U) is a weak α-emitter (4.197 MeV) with a half-life of 4.47 × 10^9 years. All manipulations and reactions should be carried out in monitored fume hoods, in a laboratory equipped with α- and β-counting equipment.

General considerations

Unless otherwise noted, all solvents and analytical-grade chemicals were purchased from commercial suppliers and used without further purification. *N*-methylacetohydroxamic acid (NMAH)[15] and 1-hydroxypiperidine-2-one (1,2-PIPOH)[27] were synthesized according to procedures published elsewhere. The sample used herein was taken from the same batches for which analytical data (^{1}H and ^{13}C NMR, CHN contents) have been reported.[15,27] Compounds were characterized at the "Plateforme d'Analyses Chimiques et de Synthèse Moléculaire de l'Université de Bourgogne - Pôle Chimie Moléculaire", the technological platform for chemical analysis and molecular synthesis (http://www.wpcm.fr). Centesimal CHN contents were obtained with a Flash EA 1112 (Thermo Scientific) CHNS analyzer. Unless otherwise noted (see the Potentiometry section), pH is defined as –log a_{H^+}. Under such circumstances, the electrode was calibrated with commercial aqueous buffers (pH = 4, 7, 10).

NMR spectroscopy. ^{1}H and ^{13}C {^{1}H} NMR spectra were recorded at 300 K using Bruker spectrometers operating either at 300 MHz (Avance III NanoBay) or 600 MHz (Bruker Avance II),

using $CDCl_3$ and D_2O as solvents. Chemical shifts in ppm downfield to tetramethylsilane were referenced internally with respect to the protio resonance of residual $CHCl_3$ in $CDCl_3$. For measurements in D_2O, an insert containing $CDCl_3$ was introduced in the NMR tubes.

Samples for DOSY experiments were prepared in D_2O. Adjustments to the desired pH were made using drops of DCl or NaOD solutions. The approximate pH was calculated from the measured pD* value with the correlation pH = pD* − 0.4 (pD* = –log [D^+] was measured with a pHc 3006 (Radiometer) semi-micro electrode calibrated with aqueous pH 4, 7, and 10 buffers). The 2D ^1H DOSY experiments were recorded at 300 K on a Bruker Avance II 600 MHz spectrometer equipped with a BBI 5 mm probe, using a LED-bipolar gradient pulse sequence (ledbpgp2s). Experimental parameters were set to 100 ms for the diffusion delay, 0.3 ms for the gradient recovery delay, and 3 ms for the eddy current recovery delay. For each data set, 16384 complex points were collected for each 30 experiments in which the gradient strength was exponentially incremented from 1 to 47.5 Gcm^{-1}. The gradient duration $\delta/2$ was adjusted to observe a near complete signal loss at 47.2 Gcm^{-1}. Typically, the $\delta/2$ delay was chosen at 0.7 ms. A 2 s recycle delay was used between scans for all data shown. The number of scans was 16 and the experiment time 24 min. 2D spectra were generated by the DOSY Module of NMRNotebook from NMRTEC[70] and the inverse Laplace transform, driven by maximum entropy, to build the diffusion dimension.[71] The spectral axis was processed with the sine-bell function, and the Fourier transform was applied in order to obtain 8000 real points. The DOSY reconstruction was realized with 192 points in the diffusion dimension and 8000 in the other dimension.

Infrared spectroscopy. Fourier-transform mid-infrared (400–4000 cm^{-1}) spectra (FT-MIR) were recorded at 4 cm^{-1} resolution on a Bruker VERTEX 70v spectrometer fitted with an A225 diamond attenuated total reflection (ATR) accessory (Bruker) and a DTGS (deuterated triglycine sulfate) detector (350–4000 cm^{-1}). ATR spectra of single crystals were collected at the same resolution with a LUMOS (Bruker) microscope equipped with a germanium ATR tip in the 650–4000 cm^{-1} range.

Raman spectroscopy. Raman spectra were collected at 2 cm^{-1} resolution with a Renishaw inVia spectrometer equipped with a 632.8 nm He-Ne laser excitation source, a 1800 grooves mm^{-1} grating, and a microscope fitted with either a ×50 (solid samples) or ×20 (liquid samples) objective. Wavenumbers were calibrated with respect to the silicon scattering line at 520(1) cm^{-1} of an internal standard, whereas an external Si reference was used periodically to check for energy drifts over time. Solid samples were deposited on a glass slide, while solutions were introduced in a stoppered fluorescence quartz cuvette of 1 cm path length (Hellma). For p[H] titration studies, 100 scans were averaged for each spectrum recorded over the range 750–1100 cm^{-1}. A combined semi-micro pHc3006 electrode and a PHM 240 ionometer, both from Radiometer, were used to measure the free proton concentration at equilibrium. Electrode calibration was performed as described in the potentiometry section. Spectral band-shape analysis with Lorentzian functions and integration were performed with the Origin 6.0 software.[72]

Synthesis

$[UO_2(NMA)_2(H_2O)]$. To an aqueous solution (5 mL) of NMAH (100 mg, 1.12 mmol) at pH 4.9 was added in one portion 141 mg (0.281 mmol) of $[UO_2(NO_3)_2(H_2O)_2]\cdot 4H_2O$. After dissolution, the pH dropped to 1.7 and the reaction mixture became orange, indicating complex formation. The pH was then adjusted to 5.1 with ca. 5 mL of a 0.1 M $N(CH_3)_4OH$ solution. Red-orange crystals deposited upon partial slow evaporation of the mother liquor. X-ray diffraction studies confirmed unambiguously the $[UO_2(NMA)_2(H_2O)]$ formula.[15] The remaining crystalline solid was recovered by filtration, washed with a minimum amount of water, and dried under vacuum. Yield: 80 mg (0.172 mmol, 61%). IR (ATR, cm^{-1}): $\tilde{\nu}$ = 2938 (v br, w), 1718 (w), 1597 (s), 1475 (s), 1419 (s), 1374 (m), 1217 (m), 1164 (s), 1034 (w), 972 (m), 896 (ν_{as}(U=O), s), 830 (ν_s(U=O), w), 752 (s), 612 (s), 595 (m), 486 (s). Raman (cm^{-1}): $\tilde{\nu}$ = 2939, 1622, 1603, 828 (ν_s(U=O), vs), 757, 221. Anal. calcd. (%) for $C_6H_{14}N_2O_7U$ (464.21 g mol^{-1}): C 15.52, H 3.04, N 6.03; found: C 15.61, H 3.06, N 6.09.

$[UO_2(PIPO)_2(H_2O)]$. PIPOH (34.57 mg, 0.30 mmol) and $[UO_2(NO_3)_2(H_2O)_2]\cdot 4H_2O$ (51.72 mg, 0.10 mmol) were dissolved in 1 mL distilled water, resulting in a deep red solution. The pH was raised to 6.2 with constant vigorous stirring, via the careful addition of 10% KOH, producing a fine, bright orange precipitate. After 30 min of continuous stirring, the mixture was placed into a refrigerator for 2 days. The precipitate was filtered, washed with 2 × 0.1 mL of fridge-cold deionized water and dried in a desiccator over silica for 3 days, resulting in a bright orange microcrystalline powder. Yield: 30.6 mg (0.059 mmol, 59%). IR (ATR, cm^{-1}): $\tilde{\nu}$ = 3144 (v br, w), 2973 (w), 2949 (w), 2873 (w), 1688 (w), 1595 (s), 1471 (m), 1440 (m), 1424 (m), 1350 (w), 1329 (w), 1312 (w), 1269(w), 1249 (w), 1207 (w), 1183 (w), 1165 (w), 1103 (m), 1066 (w), 974 (w), 905 (ν_{as}(U=O), s), 877 (m), 823 (ν_s(U=O), w), 721 (s), 652 (m), 590 (m), 530 (m), 499 (s). Raman (cm^{-1}): $\tilde{\nu}$ =1424, 975, 878, 835 (ν_s(U=O), vs), 725, 512, 227. Anal. calcd. (%) for $C_{10}H_{18}N_2O_7U$ (516.29 g mol^{-1}): C 23.26, H 3.51, N 5.43; found: C 23.69, H 3.69, N 5.45.

Orange X-ray quality crystals were obtained likewise by slow evaporation of an aqueous solution at pH ~ 5. A small amount was collected after 3 weeks, washed with one drop of distilled water, air-dried, and characterized by FT-MIR and Raman spectroscopy. Spectra data were essentially identical to those reported for the microcrystalline powder.

X-ray crystallography

Crystal data were collected on a Nonius Kappa diffractometer equipped with an Appex II detector. A suitable specimen (0.40 × 0.30 × 0.17 mm) was selected and mounted on a Mylar loop with oil. The X-ray source was a graphite monochromated Mo K_α radiation (λ = 0.71073 Å) from a sealed tube. Data were measured using ϕ and ω scans, under a liquid nitrogen jet stream (Oxford Cryosystems). Cell parameters were retrieved and refined with the SAINT software (release 8.38a).[73] Data reduction was performed using the same program, which corrects for Lorentz polarization. Structures were solved by

direct methods using the ShelXT software[74] and then refined by full-matrix least-squares on F^2 using ShelXL (release 2017/1),[75] both routines being implemented in the Olex2 environment.[76] All non-hydrogen atoms were refined anisotropically. Hydrogen atom positions were calculated geometrically and refined using the riding model, excepted those on water molecule, which were located in the Fourier difference maps. Their positional parameters were fixed with $U_{iso}(H) = 1.2U_{eq}(O)$. CCDC-1579042 for $[UO_2(PIPO)_2(H_2O)]$ contains the supplementary crystallographic data for this paper. These data can be obtained free of charge from The Cambridge Crystallographic Data Centre via www.ccdc.ac.uk/data_request/cif.

Crystal data for $[UO_2(PIPO)_2(H_2O)]$. $C_{10}H_{18}N_2O_7U$, M_r = 516.29 g mol^{-1}, monoclinic space group $P2_1/c$ (No. 14), a = 6.472(3) Å, b = 27.71(1) Å, c = 8.310(3) Å, β = 110.610(9)°, V = 1394.9(9) Å^3, Z = 4, ρ_{calcd} = 2.458 g cm^{-3}, T = 115(1) K, μ(Mo Kα) = 11.669 mm^{-1} (λ = 0.710730 Å), 31311 reflections measured (2.94° ≤ 2θ ≤ 55.34°), 3243 unique (R_{int} = 0.0412), 3156 used with $I > 2\sigma(I)$, 181 parameters and 0 restraint. Final R_1 = 0.0273 ($I > 2\sigma(I)$), wR_2 = 0.0600 (all data), min./max. residual electron density = −2.351/2.013 e Å^{-3}.

Potentiometry

Solution preparations. All solutions were prepared with boiled and argon-saturated double-deionized high-purity water (18.2 MΩ cm) obtained from a Maxima (USF Elga) cartridge system designed for trace analysis. The 0.1 M HNO_3 and carbonate-free KOH solutions were prepared from Merck concentrates (Titrisol®) and were standardized by titrating against oven-dried (120 °C for 2 h) Tris buffer (Aldrich-Sigma, 99.9%) and potassium hydrogen phthalate (Aldrich-Sigma, 99.99%), respectively. Equivalence points were calculated by the second-derivative method. The concentration of the standardized solutions corresponded to the average of at least five replicates and was known with a relative precision better than 0.15%. They were stored under purified argon using Ascarite II (Acros, 20–30 mesh) scrubbers in order to prevent absorption of carbon dioxide. The uranyl mother solution (c = 0.0511(2) M) was prepared by dissolving an exactly weighted amount of $[UO_2(NO_3)_2(H_2O)_2]\cdot 4H_2O$ in 0.100 M HNO_3. The purity of the uranium salt was checked independently by polarography in a 0.1 M KNO_3 solution using a Voltalab PST050 (Radiometer) potentiostat and a 150 VA (Radiometer) dropping mercury electrode in conjunction with a XR110 (Radiometer) KCl-saturated calomel electrode and a platinum counter-electrode. The calibration line was built by analyzing 5 solutions obtained by dilution of a certified 1 g L^{-1} ICP standard (Spex). Ligand stock solutions were prepared by careful weighing with a Precisa 262SMA-FR balance (precision: ± 0.01 mg).

Titration procedure. Acid-base titrations were carried out in a water-jacketed cell connected to a Lauda RE106 water circulator ensuring a constant temperature of 298.2(2) K. Magnetically stirred solutions were maintained under an argon stream to exclude CO_2 from the laboratory atmosphere. Titrations were conducted in 0.1 M KNO_3 solutions to keep the ionic strength approximately constant. The equipment and detailed procedure have been described elsewhere.[77-78] Titrant aliquots were delivered through a polypropylene line from a calibrated automatic ABU901 (Radiometer) 10-mL piston burette. Volumes were corrected according to a linear calibration function obtained by weighing known quantities of water and by taking into account the buoyancy effect. Potentials were recorded at ± 0.1 mV resolution with glass-bulb (XG100, Radiometer) and calomel (XR110, Radiometer) electrodes connected to a PHM 240 ionometer (Radiometer). The reference half-cell was separated from the test solution by a sintered-glass salt bridge filled with 0.1 M KNO_3. Both instruments were controlled by the HRT Acid–Base Titration software written by Mustin.[79]

Prior to each experiment, the glass electrode was calibrated as a hydronium ion concentration probe (p[H] = –log [H_3O^+]) by titrating 4.000 mL of standardized 0.1 M HNO_3 diluted in 25 mL of 0.1 M KNO_3 with 9.010 mL of 0.1 M standardized KOH, added in 0.120 mL increments. Calibration data (1.8 ≤ p[H] ≤ 11.9) were processed according to the four-parameter extended Nernst equation (eqn (8)), which takes into account the standard potential (E^0), the Nernst slope (S), and the correction terms accounting for the changes in liquid junction potential in the acidic (J_a) and alkaline (J_b) region.[80] In addition, the base-concentration factor was also allowed to refine, whereas the ionic product of water was fixed ($K_w = 10^{-13.78}$ M^2 in 0.1 M KNO_3 at 298.15 K).[49,81]

$$E_{mes} = E^0 + S \log [H^+] + J_a [H^+] + J_b K_w [H^+]^{-1} \quad (8)$$

In a typical experiment, *ca*. 0.1 mmol of ligand was dissolved in 25 mL of supporting electrolyte solution acidified with 0.1 M HNO_3 to reach an initial p[H] of 1.8–2. The uranyl solution was introduced afterwards in order to reach a ligand-over-metal concentration ratio of 1 or 2. The reaction mixture was then allowed to equilibrate for several minutes by monitoring the time dependence of the potential before starting the incremental addition of base. Stable readings were obtained when the fluctuation did not exceed 0.1 mV within a series of N_{ps} = 100 replicate measurements taken at a sampling rate of ca. 0.8 s per point (N_{ps} was set to 25 for electrode calibration and 50 for protonation constant measurements).[79] This stability criterion was reached after a few minutes following the injection of titrant. Moreover, the thermodynamic reversibility was checked by cycling the titrations from low to high p[H] and *vice versa*.

The collected potential readings were converted into p[H] values with the help of a Microsoft Excel spreadsheet by iterative solving of a rearranged form of eqn (8). For each system, at least three individual titration curves were merged in order to perform a global fit by the weighed nonlinear least-squares program Hyperquad 2013.[52] The weights were derived from the estimated errors in p[H] ($\sigma_{p[H]}$ = 0.003) and delivered volume (σ_V = 0.005 mL). For metal-ligand titrations, the protonation constant of the ligand and the equilibrium constants for uranyl hydrolysis (Table S8, see ESI†)[53] were treated as fixed parameters. The goodness of fit was assessed through the scaled standard deviation of the residuals (σ), which has an expected value of one in the absence of systematic

errors assuming a correct weighting scheme. Data sets and models were accepted when σ was lower than 2. The final accepted values are reported together with the corresponding standard deviation indicated in parentheses as the last significant digit. Distribution diagrams were computed with the Hyss program.[82]

Absorption spectrophotometry

Spectrophotometric titrations. Visible absorption spectra were recorded *in situ* as a function of p[H] with a Cary 50 Probe (Varian) spectrophotometer equipped with an immersion probe of 1 cm path length made of SUPRASIL® 300 (Hellma, reference 661.202). The same titration cell and electrode calibration procedure as described above were used. Prior to each titration, the reference spectrum of the 0.1 M KNO_3 supporting electrolyte solution was acquired in the 320−650 nm range. The standard deviation of the measured absorbance for the baseline was constant over the entire wavelength region and did not exceed 0.002 absorbance unit.

Aliquots of base were added manually with the help of a Gilmont micropipette (2 μL resolution) to a *ca*. 1.3 mM ligand solution containing half and equivalent of uranyl nitrate. Enough time was allowed after the addition of each base increment in order to reach the equilibrium. The potential-drift criterion was set at dE/dt < 0.1 mV min^{-1}. The collection of absorption spectra was repeated with 2 min delays between two consecutive measurements until superimposable spectra were obtained, the optical densities being below 0.5 units. For each titration point, the pH-meter readings were stable in less than 2 min, and no more than two spectral recordings were required.

Data sets for at least 3 independent titrations were merged before performing a multiwavelength global fit with the Hyperquad 2006 program, following a refinement strategy described in detail elsewhere.[83] The selected weighing scheme ($\sigma_{p[H]}$ = 0.003, σ_V = 0.005 mL, σ_A = 0.002 a.u.) based on the error-propagation rule seeks to give an approximately equal contribution to the overall residual sum of squares to both potentiometric and spectrophotometric data. The extinction coefficients for free UO_2^{2+} were fixed in order to reach convergence. The goodness-of-fit was assessed by the overall standard deviation (σ < 1.5), the visual inspection of the residuals, and by the physical meaning of the calculated electronic absorption spectra.

Diffuse reflectance spectroscopy. Diffuse reflectance spectra of pure microcrystalline complexes were acquired between 200 and 2500 nm on a CARY 5000 (Agilent) UV–vis–NIR spectrophotometer fitted with a Praying Mantis™ accessory (Harrick), the baseline being recorded on dry barium sulfate (Avocado, <99%). Corrected reflectance data were converted to $f(R)$ values using the Kubelka-Munk function expressed as $f(R) = (1 - R)^2/2R$.

Isothermal titration calorimetry (ITC)

Calorimetric measurements were performed at 298.15 K using a TAM III (TA Instruments) isothermal titration calorimeter equipped with a 4 mL nanocalorimeter (part n° 3201) immersed into an oil-filled thermostat (ΔT < 80 μK with a drift of less than 6 μK over 24 h). The performance of the instrument was evaluated by measuring the dilution heat of a 10.075% w/w 1-propanol/water mixture into pure water. The experimental average value for two replicates determined at 298.15 K (Q = 2.57(3) J g^{-1} of propanol-1) compared very well with that preconized by IUPAC (Q = 2.57(2) J g^{-1}).[84]

The glass titration vessel was loaded with 0.800 mL of an aqueous ligand solution (3.33 mM) containing 0.1 M KNO_3 as supporting electrolyte. The reference vessel was filled with 0.800 mL of the same ligand solution and 0.100 mL of 0.1 M KNO_3. The titration vessel was maintained under constant stirring with a gold propeller during all experiments. The endpoint was reached after addition of 30 increments of 5 μL each of a standardized 0.05 M KOH solution by a programmable Hamilton syringe pump. A waiting time of 30 min between two consecutive injections was long enough for allowing the signal to reach the baseline.

Raw thermal data were corrected for dilution effects by performing separate blank titrations using the same experimental conditions but without the ligand. Protonation enthalpies were calculated from calorimetric data by the HypCal program.[85] Values of the protonation constants obtained by potentiometry were fixed during the refinement, as well as the water autoprotolysis constant (log K_w = −13.78, I = 0.1 M KNO_3, T = 298.15 K)[49,81] and the water dissociation enthalpy ($\Delta_r H_{00-1}$ = 56.48 kJ mol^{-1}, I = 0.1 M, T= 298.15 K).[49] The NIST-recommended value is in excellent agreement with our own determination in duplicate (–56.4(1) kJ mol^{-1}) by neutralizing $HClO_4$ by NaOH in 0.1 M $NaClO_4$.

Affinity capillary electrophoresis (ACE)

The uranyl perchlorate stock solution (0.1 M in 0.63 M $HClO_4$) was obtained by dissolving $[UO_2(NO_3)_2(H_2O)_2]\cdot 4H_2O$ (Fluka puriss., ≥99%) in 12 M $HClO_4$ (Merck Suprapur) and evaporating the resulting solution to almost dryness on a sand bath. The residue was dissolved in concentrated $HClO_4$ and evaporated again. This last operation was repeated three times. The final uranyl concentration was determined by liquid counting scintillation method. Concentrated perchloric acid (Sigma-Aldrich, 60%) was diluted in water to the required concentration. The exact titer was determined by acid-base titration with a certified NaOH solution. Sodium perchlorate (≥99%) was purchased from Fluka-Merck and dimethyl sulfoxide (DMSO) (≥99.9%) from Sigma-Aldrich. All solutions were prepared with deionized high-purity water (18.2 MΩ cm) produced by a Millipore Direct Q apparatus. For all samples analyzed by ACE, p[H] values were measured with a GLP-21 (Crison, France) pH-meter connected to a combined glass electrode calibrated in concentration units.

In order to avoid hydrolysis and further polymerization of the uranyl ion, which could potentially lead to the formation of additional species and/or to the modification of the uranyl mobility, a 0.1 M (H,Na)ClO_4 solution of p[H] = 2.50 ± 0.05 was used as background electrolyte (BGE). Under such conditions and a total uranyl concentration of 0.1 mM, the contribution of hydrolyzed and polymeric uranyl species is negligible.[53-54]

Electrophoregrams were acquired on a P/ACE MDQ (Beckman Coulter) instrument equipped with a 0−30 kV high-voltage built-in power supply and a diode array detector. UV direct detection at 200 and 250 nm was used in this work. The fused silica capillary (Beckman Instruments) of 50 μm internal diameter, 375 μm outer diameter, 31.2 cm total length (L), and 21 cm effective separation length (l), was housed in an interchangeable cartridge with a circulating liquid coolant that maintained the temperature at 25 °C. Before use, the capillary was preconditioned by successive washes with 1 M and then 0.1 M NaOH solutions, deionized water, and the buffer solution under study. It was rinsed for 3 minutes at a pressure of 15 psi with the buffer solution between two runs and kept filled with deionized water overnight. Solutions were injected for 4 s at a pressure of 0.5 psi at the negative capillary end, in the normal polarity mode. The applied potential was 5 kV, as required by the Ohm's law. The current value was about 60 μA. Separations were performed at constant forward pressure of 0.2 psi. Each measurement was repeated at least three times. Data acquisition and processing were carried out with the Karat 32 software from Beckman Coulter.

The electrophoretic mobility μ_{obs} ($m^2\ s^{-1}\ V^{-1}$) was calculated by using expression (9),

$$\mu_{\mathrm{obs}} = \frac{L\,l}{V}\left(\frac{1}{t} - \frac{1}{t_{\mathrm{eof}}}\right) \qquad (9)$$

where L is the total capillary length (m), l is the distance between the capillary inlet and the detection window (m), V is the applied voltage (V), t is the migration time of the studied species (s), and t_{eof} is the migration time of DMSO (s), used as a neutral marker for electro-osmotic flow determination. μ_{obs} versus total ligand concentration curves were fit with the Marquardt nonlinear least-squares algorithm implemented in the HypNMR program.[68]

Conflicts of interest

There are no conflicts to declare.

Acknowledgements

The Centre National de la Recherche Scientifique (CNRS), the Conseil Régional de Bourgogne (CRB, program PARI II CDEA), the European Regional Development Fund (FEDER), the program "Défi NEEDS Environnement" (project ACTISOL) are gratefully acknowledged for their financial support. A.S. and T.F. are in debt to the CRB and FEDER for granting them a post-doctoral fellowship (grant numbers 2012-9201AAO049S02778 and 2016-9201AAO049S01737). P.J. thanks the CNRS and the CRB for a PhD fellowship (grant number 2009-9201AAO037S03746). We thank Marie-José Penouilh, Marcel Soustelle, and Dr Michel Piquet for their technical assistance, and Prof. Istvan Banyai (University of Debrecen) for processing the DOSY spectra.

Notes and references

1 P. Crançon and J. van der Lee, *Radiochim. Acta*, 2003, **92**, 673-679.
2 D. M. Sherman, C. L. Peacock and C. G. Hubbard, *Geochim. Cosmochim. Acta*, 2008, **72**, 298-310.
3 S. Mishra, S. Maity, S. Bhalke, G. Pandit, V. Puranik and H. Kushwaha, *J. Radioanal. Nucl. Chem.*, 2012, **294**, 97-102.
4 Z. Wang, J. M. Zachara, J.-F. Boily, Y. Xia, T. C. Resch, D. A. Moore and C. Liu, *Geochim. Cosmochim. Acta*, 2011, **75**, 2965-2979.
5 J. R. Brainard, B. A. Strietelmeier, P. H. Smith, P. J. Langston-Unkefer, M. E. Barr and R. R. Ryan, *Radiochim. Acta*, 1992, **58-59**, 357-364.
6 M. Bouby, I. Billard, J. MacCordick and I. Rossini, *Radiochim. Acta*, 1998, **80**, 95-100.
7 J. C. Renshaw, V. Halliday, G. D. Robson, A. P. J. Trinci, M. G. Wiebe, F. R. Livens, D. Collison and R. J. Taylor, *Appl. Environ. Microbiol.*, 2003, **69**, 3600-3606.
8 C. E. Ruggiero, H. Boukhalfa, J. H. Forsythe, J. G. Lack, L. E. Hersman and M. P. Neu, *Environ. Microbiol.*, 2005, **7**, 88-97.
9 S. W. Frazier, R. Kretzschmar and S. M. Kraemer, *Environ. Sci. Technol.*, 2005, **39**, 5709-5715.
10 D. Wolff-Boenisch and S. J. Traina, *Chem. Geol.*, 2007, **242**, 278-287.
11 A. M. Albrecht-Gary and A. L. Crumbliss, in *Metal Ions in Biological Systems. Iron Transport and Storage in Microorganisms, Plants, and Animals*, eds. A. Sigel and H. Sigel, Marcel Dekker, New York, 1998, vol. 35, pp. 239-327.
12 A. Stintzi and K. N. Raymond, in *Molecular and Cellular Iron Transport*, ed. D. E. Templeton, Marcel Dekker, New York, 2001, pp. 273-319.
13 E. A. Dertz and K. N. Raymond, in *Iron Transport in Bacteria*, eds. J. H. Crosa, A. R. Mey and S. Payne, ASM Press, Washington, DC, 2004, pp. 5-17.
14 D. J. Raines, T. J. Sanderson, E. J. Wilde and A. K. Duhme-Klair, in *Reference Module in Chemistry, Molecular Sciences and Chemical Engineering*, Elsevier, 2015.
15 S. Brandès, A. Sornosa-Ten, Y. Rousselin, M. Lagrelette, C. Stern, A. Moncomble, J.-P. Cornard and M. Meyer, *J. Inorg. Biochem.*, 2015, **151**, 164-175.
16 S. P. Sippl and H. L. Schenck, *Magn. Reson. Chem.*, 2013, **51**, 72-75.
17 D. A. Brown, W. K. Glass, R. Mageswaran and S. A. Mohammed, *Magn. Reson. Chem.*, 1991, **29**, 40-45.
18 S. P. Sippl, P. B. White, C. G. Fry, S. E. Volk, L. Ye and H. L. Schenck, *Magn. Reson. Chem.*, 2016, **54**, 46-50.
19 B. Kurzak, H. Kozłowski and E. Farkas, *Coord. Chem. Rev.*, 1992, **114**, 169-200.
20 R. Codd, *Coord. Chem. Rev.*, 2008, **252**, 1387-1408.
21 I. May, R. J. Taylor, I. S. Denniss, G. Brown, A. L. Wallwork, N. J. Hill, J. M. Rawson and R. Less, *J. Alloys Compd.*, 1998, **275-277**, 769-772.
22 P. Govindan, S. Sukumar and R. V. Subba Rao, *Desalination*, 2008, **232**, 166-171.
23 T. Terencio, J. Roithová, S. Brandès, Y. Rousselin, M.-J. Penouilh and M. Meyer, *Inorg. Chem.*, 2018, **57**, 1125-1135.
24 A. A. H. Pakchung, C. Z. Soe, T. Lifa and R. Codd, *Inorg. Chem.*, 2011, **50**, 5978-5989.
25 S. Dhungana, M. J. Miller, L. Dong, C. Ratledge and A. L. Crumbliss, *J. Am. Chem. Soc.*, 2003, **125**, 7654-7663.
26 L. Dong and M. J. Miller, *J. Org. Chem.*, 2002, **67**, 4759-4770.

27 P. Jewula, J.-C. Berthet, J.-C. Chambron, Y. Rousselin, P. Thuéry and M. Meyer, *Eur. J. Inorg. Chem.*, 2015, 1529-1541.
28 L. Panizzi, G. Di Maio, P. A. Tardella and L. d'Abbiero, *Ric. Sci.*, 1961, **1**, 312-318.
29 P. Jewula, J.-C. Chambron, M.-J. Penouilh, Y. Rousselin and M. Meyer, *RSC Adv.*, 2014, **4**, 22743-22754.
30 F. H. Allen, *Acta Crystallogr., Sect. B*, 2002, **58**, 380-388.
31 M. A. Silver, W. L. Dorfner, S. K. Cary, J. N. Cross, J. Lin, E. J. Schelter and T. E. Albrecht-Schmitt, *Inorg. Chem.*, 2015, **54**, 5280-5284.
32 P. F. Weck, C.-M. S. Gong, E. Kim, P. Thuéry and K. R. Czerwinski, *Dalton Trans.*, 2011, **40**, 6007-6011.
33 R. Centore, G. De Tommaso, M. Iuliano and A. Tuzi, *Acta Crystallogr., Sect. C*, 2007, **63**, m253-m255.
34 U. Casellato, P. A. Vigato, S. Tamburini, R. Graziani and M. Vidali, *Inorg. Chim. Acta*, 1984, **81**, 47-54.
35 S. Chakraborty, S. Dinda, R. Bhattacharyya and A. K. Mukherjee, *Z. Kristallogr.*, 2006, **221**, 606-611.
36 D. K. Hazra, S. Dinda, M. Helliwell, R. Bhattacharyya and M. Mukherjee, *Z. Kristallogr.*, 2009, **224**, 544-550.
37 J. Casellato, P. A. Vigato, S. Tamburini, R. Graziani and M. Vidali, *Inorg. Chim. Acta*, 1983, **72**, 141-147.
38 M. Hojjatie, S. Muralidharan, P. S. Bag, C. G. Panda and H. Freiser, *Iran. J. Chem. Chem. Eng.*, 1995, **14**, 81-89.
39 K. Nakamoto, *Infrared and Raman Spectra of Inorganic and Coordination Compounds*, Wiley, New York, 1970.
40 W. L. Smith and K. N. Raymond, *J. Inorg. Nucl. Chem.*, 1979, **41**, 1431-1436.
41 J. R. Bartlett and R. P. Cooney, *J. Mol. Struct.*, 1989, **193**, 295-300.
42 L. Mullen, C. Gong and K. Czerwinski, *J. Radioanal. Nucl. Chem.*, 2007, **273**, 683-688.
43 C.-M. S. Gong, F. Poineau and K. R. Czerwinski, *Radiochim. Acta*, 2007, **95**, 439-450.
44 J. Wiebke, A. Moritz, M. Glorius, H. Moll, G. Bernhard and M. Dolg, *Inorg. Chem.*, 2008, **47**, 3150-3157.
45 J. Wiebke, A. Weigand, D. Weissmann, M. Glorius, H. Moll, G. Bernhard and M. Dolg, *Inorg. Chem.*, 2010, **49**, 6428-6435.
46 D.-Y. Chung, E.-K. Choi, E.-H. Lee and K.-W. Kim, *J. Radioanal. Nucl. Chem.*, 2011, **289**, 315-319.
47 B. Monzyk and A. L. Crumbliss, *J. Org. Chem.*, 1980, **45**, 4670-4675.
48 E. Farkas, E. Kozma, M. Petho, K. M. Herlihy and G. Micera, *Polyhedron*, 1998, **17**, 3331-3342.
49 A. E. Martell, R. M. Smith and R. J. Motekaitis, *NIST Critically Selected Stability Constants of Metal Complexes Database*, (2004) NIST Standard Reference Database No. 46, Gaithersburg, MD.
50 A. Alagha, L. Parthasarathi, D. Gaynor, H. Müller-Bunz, Z. A. Starikova, E. Farkas, E. C. O'Brien, M.-J. Gil and K. B. Nolan, *Inorg. Chim. Acta*, 2011, **368**, 58-66.
51 A. E. Fazary, *J. Chem. Eng. Data*, 2005, **50**, 888-895.
52 P. Gans, A. Sabatini and A. Vacca, *Talanta*, 1996, **43**, 1739-1753.
53 I. Grenthe, J. Fuger, R. J. M. Konings, R. J. Lemire, A. B. Muller, C. Nguyen-Trung and H. Wanner, *Chemical Thermodynamics of Uranium*, 2nd edn., OECD Nuclear Energy Agency, Paris, 2004.
54 R. Guillaumont, T. Fanghänel, J. Fuger, I. Grenthe, V. Neck, D. A. Palmer and M. H. Rand, *Update on the Chemical Thermodynamics of Uranium, Neptunium, Plutonium, Americium and Technetium*, Elsevier, Amsterdam, 2003.
55 B. Perlmutter-Hayman, *Acc. Chem. Res.*, 1986, **19**, 90-96.
56 J. Hamacek, M. Borkovec and C. Piguet, *Dalton Trans.*, 2006, 1473-1490.
57 F. Quilès, C. Nguyen-Trung, C. Carteret and B. Humbert, *Inorg. Chem.*, 2011, **50**, 2811-2823.
58 C. Nguyen-Trung, G. M. Begun and D. A. Palmer, *Inorg. Chem.*, 1992, **31**, 5280-5287.
59 S. Topin, J. Aupiais, N. Baglan, T. Vercouter, P. Vitorge and P. Moisy, *Anal. Chem.*, 2009, **81**, 5354-5363.
60 V. Sladkov, *Electrophoresis*, 2010, **31**, 3482-3491.
61 F. Varenne, M. Bourdillon, M. Meyer, Y. Lin, M. Brellier, R. Baati, L. J. Charbonnière, A. Wagner, E. Doris, F. Taran and A. Hagège, *J. Chromatogr. A*, 2012, **1229**, 280-287.
62 V. Sladkov, *J. Chromatogr. A*, 2013, **1289**, 133-138.
63 V. Sladkov, *J. Chromatogr. A*, 2013, **1276**, 120-125.
64 A. R. Timerbaev and R. M. Timerbaev, *Trends Anal. Chem.*, 2013, **51**, 44-50.
65 V. Sladkov, *Electrophoresis*, 2016, **37**, 2558-2566.
66 R. Konášová, J. J. Dytrtová and V. Kašička, *J. Sep. Sci.*, 2016, **39**, 4429-4438.
67 C. Jiang and D. W. Armstrong, *Electrophoresis*, 2010, **31**, 17-27.
68 C. Frassineti, S. Ghelli, P. Gans, A. Sabatini, M. S. Moruzzi and A. Vacca, *Anal. Biochem.*, 1995, **231**, 374-382.
69 R. Mills, *J. Phys. Chem.*, 1973, **77**, 685-688.
70 *NMRNotebook*, NMRTEC SAS, Illkirch-Graffenstaden, France. http://www.nmrtec.com/software/nmrnotebook
71 M. A. Delsuc and T. E. Malliavin, *Anal. Chem.*, 1998, **70**, 2146-2148.
72 *Origin 6.0*, Microcal Software Inc., Northampton, MA.
73 *SAINT: Area-Detector Integration Sofware*, (2013) Bruker, Madison, Wisconsin, USA.
74 G. M. Sheldrick, *Acta Crystallogr., Sect. A*, 2015, **71**, 3-8.
75 G. Sheldrick, *Acta Crystallogr., Sect. C*, 2015, **71**, 3-8.
76 O. V. Dolomanov, L. J. Bourhis, R. J. Gildea, J. A. K. Howard and H. Puschmann, *J. Appl. Crystallogr.*, 2009, **42**, 339-341.
77 F. Cuenot, M. Meyer, E. Espinosa, A. Bucaille, R. Burgat, R. Guilard and C. Marichal-Westrich, *Eur. J. Inorg. Chem.*, 2008, 267-283.
78 E. Ranyuk, A. Uglov, M. Meyer, A. Bessmertnykh-Lemeune, F. Denat, A. Averin, I. Beletskaya and R. Guilard, *Dalton Trans.*, 2011, **40**, 10491-10502.
79 G. Naja, C. Mustin, B. Volesky and J. Berthelin, *Water Res.*, 2005, **39**, 579-588.
80 A. Avdeef and J. J. Bucher, *Anal. Chem.*, 1988, **50**, 2137-2142.
81 I. Kron, S. L. Marshall, P. M. May, G. Hefter and E. Königsberger, *Monatsh. Chem.*, 1995, **126**, 819-837.
82 L. Alderighi, P. Gans, A. Ienco, D. Peters, A. Sabatini and A. Vacca, *Coord. Chem. Rev.*, 1999, **184**, 311-318.
83 M. Meyer, R. Burgat, S. Faure, B. Batifol, J.-C. Hubinois, H. Chollet and R. Guilard, *C. R. Chimie*, 2007, **10**, 929-947.
84 I. Wadsö and R. N. Goldberg, *Pure Appl. Chem.*, 2001, **73**, 1625-1639.
85 G. Arena, P. Gans and C. Sgarlata, *Anal. Bioanal. Chem.*, 2016, **408**, 6413-6422.